Materials Transactions, Vol. 44, No. 1 (2003) pp. 94 to 103

Characterization and Determination of Elastic Property of High-Density Nanocrystalline Gold Prepared by Gas-Deposition Method

Hisanori Tanimoto[1], Seiji Sakai[1,*], Eiji Kita[2] and Hiroshi Mizubayashi[1]

[1]*Institute of Materials Science, University of Tsukuba, Tsukuba, 305-8573, Japan*
[2]*Institute of Applied Physics and Center for Tsukuba Advanced Research Alliance (TARA), University of Tsukuba, Tsukuba, 305-8573, Japan*

Nanocrystalline (n-) Au specimens with the density of $19400 \pm 200\,kg/m^3$ were prepared by the gas deposition method. Since rearrangement of n-Au particles on the specimen surfaces takes place just after landing, the grain boundary energy of $(0.3 \pm 0.15)\,J/m^2$ is comparable with $0.45\,J/m^2$ reported for the bulk polycrystalline (p-) Au, and the concentration of vacancy type defects is about 15×10^{-4} in the as deposited state decreasing with the grain growth. The Young modulus observed at 10 K is almost the same to that estimated under the condition that stresses applied to the constituent crystallites are equal among all the crystallites while strains are variable.

(Received September 27, 2002; Accepted November 18, 2002)

Keywords: *nanocrystalline gold, grain boundary energy, Young modulus, vacancy concentration, gas deposition method*

1. Introduction

Nanocrystalline (n-) metals[1)] are considered as composite materials composed of nanocrystallites and the grain boundary (GB) regions, where new properties such as superior magnetism[2)] and super-plasticity[3)] have been reported. The characteristic properties of n-metals such as the grain growth temperature, the excess vacancy type defects and the elastic response are disputed. The grain growth in n-Au specimens containing considerable pores is reported to be strongly retarded.[4)] On the other hand, it is indicated that the grain growth in the high-density n-Pd[5)] and n-Au[6)] specimens starts slightly above room temperature. For n-Fe specimens, the size-dependent grain growth is reported.[7)] Theoretically, it is suggested that the grain growth process in n-metals would be retarded in comparison with that in the bulk polycrystalline (p-) metals when the excess vacancy type defects contained in the GB regions should move into the constituent crystallites.[8,9)] The excess vacancy type defects may play an important role on the thermal stability of the high-density n-metal, as well as the grain growth process.

The very low elastic modulus reported in the pioneer works[10–12)] of n-metals is probably due to pores contained in the n-metal specimens. Recently, Sanders *et al.*[13–15)] studied on n-Cu and n-Pd specimens with the relative density, ρ/ρ_0 (ρ_0: the full density), of 82–98%, and reported that the Young modulus extrapolated to the full density state shows good agreement with the bulk value. Qin *et al.*[16)] reported that in n-Ag specimens with ρ/ρ_0 of 90–98%, the Young modulus extrapolated to the full density state is lower by about 15% than the bulk value. In our previous work[17)] on n-Au specimens with $\rho/\rho_0 > 98\%$, the Young modulus is about 90% of the bulk value. Ultrasonic wave velocity measurements on high-density n-Fe and n-Ti specimens also show that the elastic moduli are about 95% of the bulk values.[18)] That is, the values of the Young modulus observed for the high-density n-metals is comparable to the intrinsic bulk values. On the other hand, the theoretical value of the Young modulus of a polycrystalline material is known to be in between ${}^{\sigma}E_0$ and ${}^{\varepsilon}E_0$, where ${}^{\sigma}E_0$ denotes the Young modulus estimated under the condition that stresses applied to the constituent crystallites are equal among all the crystallites while strains are variable, and ${}^{\varepsilon}E_0$ denotes the Young modulus estimated under the opposite condition. ${}^{\sigma}E_0$ and ${}^{\varepsilon}E_0$ are given by the following eqs. (1) and (2),

$$1/{}^{\sigma}E_0 = \sum_{\langle hkl \rangle} (R_{\langle hkl \rangle}/E_{\langle hkl \rangle}), \tag{1}$$

and

$${}^{\varepsilon}E_0 = \sum_{\langle hkl \rangle} (R_{\langle hkl \rangle} E_{\langle hkl \rangle}), \tag{2}$$

where $R_{\langle hkl \rangle}$ and $E_{\langle hkl \rangle}$ denote the fractional volume and the Young modulus of the constituent $\langle hkl \rangle$ crystallites, and Young modulus of the GB region is assumed to be the bulk value. The mean value between ${}^{\sigma}E_0$ and ${}^{\varepsilon}E_0$ is called as the Young modulus under the Hill's assumption, ${}^{\mathrm{Hill}}E_0$. It is noted that ${}^{\sigma}E_0 < {}^{\varepsilon}E_0$ is expected for a metal with the anisotropic Young modulus, and the Young modulus of Au strongly depends on the crystallographic direction.[19)] Then, one may expect that the Young modulus of n-Au specimens can be compared with ${}^{\sigma}E_0$ and ${}^{\varepsilon}E_0$ giving an insight into the deformation mode in n-metals. In the present work, we evaluated the Young modulus of the high-density n-Au specimens and discussed in a view point of deformation mode.

2. Experimental Procedures

High-density n-Au specimens were prepared by the gas deposition (GD) method.[20,21)] The GD apparatus was composed of an evaporation chamber, a deposition chamber and a helium circulation system with purification columns,[17)] where the two chambers were connected by a narrow pipe (the transfer pipe, hereafter). Prior to deposition, the apparatus was evacuated down to 10^{-4} Pa for one day to

*Present address: Takasaki-branch, Advanced Science Research Center, Japan Atomic Energy Research Institute, Watanuki, Takasaki 370-1292, Japan.

minimize outgassing from the inner walls. During the deposition, the helium gas circulation system was in operation, where the evaporation and deposition chambers were evacuated by rotary vacuum pumps and a He gas was simultaneously supplied to the evaporation chamber at the rate of 35 L/min. The He gas pressure in the evaporation chamber was maintained at 66.7 kPa, and that in the deposition chamber at 133 Pa. The monitored purity of He gas was better than 99.9999% during the deposition, because pure He gas is necessary for obtaining contamination-free and pore-free n-Au specimens. In the evaporation chamber, 99.999% pure Au in a graphite crucible was heated by an RF-induction heater, where n-Au particles were formed by the inert-gas condensation process just above the Au melt. The n-Au particles were suctioned by the transfer pipe and immediately transferred onto a glass substrate in the deposition chamber by a He gas jet flow in the transfer pipe. In the previous works,[17,22] an agglomeration of n-Au particles took place in the transfer pipe with a tapered-off nozzle. Here, we used a straight transfer pipe in order to avoid the undesirable agglomeration.

A model calculation[23] for helium gas flow in the present straight transfer pipe with 1.8 mm inner diameter showed that the flow speed at the inlet and outlet was about 200 and 350 m/s, respectively, where an adiabatic compressible flow in the straight pipe at Fanning friction factor of 0.004 is assumed. In the present experiment, a mass fraction of Au particles against the helium gas flow was less than 10^{-3}. In this case, Au particles with diameter less than several tens nm are accelerated to a speed of the helium gas flow in a few μs,[24] and are transferred onto a substrate in a few ms. In the present experiment, the deposition rate of the n-Au particles was controlled by the Au melt temperature, T_L. Figure 1(a) shows T_L as a function of the RF-induction power, P_i, where T_L was measured by the pyrometer. Since T_L increases from 1670 to 1850 K with increasing P_i from 3.6 to 4.8 kW, the deposition rate of n-Au particles can be denoted by P_i instead of T_L.

In order to avoid a grain growth during the deposition, the temperature of the glass substrate was kept below about 270 K using a cold stage. Ribbon shape n-Au specimens 0.02–0.1 mm thick, 1 mm wide and 23 mm long were prepared by controlling the position of the glass substrate. The specimen face of 1 mm wide and 23 mm long will be referred to as the specimen flat-surface, hereafter. To detach the n-Au specimen from the glass substrate, a water drop was given on one edge of the specimen and the edge corner was gently scratched with a thin razor blade. Then, the n-Au specimen spontaneously peeled off from the glass substrate. The density of n-Au specimens was measured by the Archimedes' method using high-purity ethanol.

A thermal gas-desorption analysis was performed up to 1100 K in a high vacuum. No degassing from the n-Au specimens was observed except for degassing of H_2O adsorbed on the specimen surfaces. No contaminations by heavy elements were detected by the electron probe micro-analyzer. The scanning tunneling microscope (STM) operating at the constant current mode was used to check the morphology of the specimen flat-surface and the cross-sectioned face.

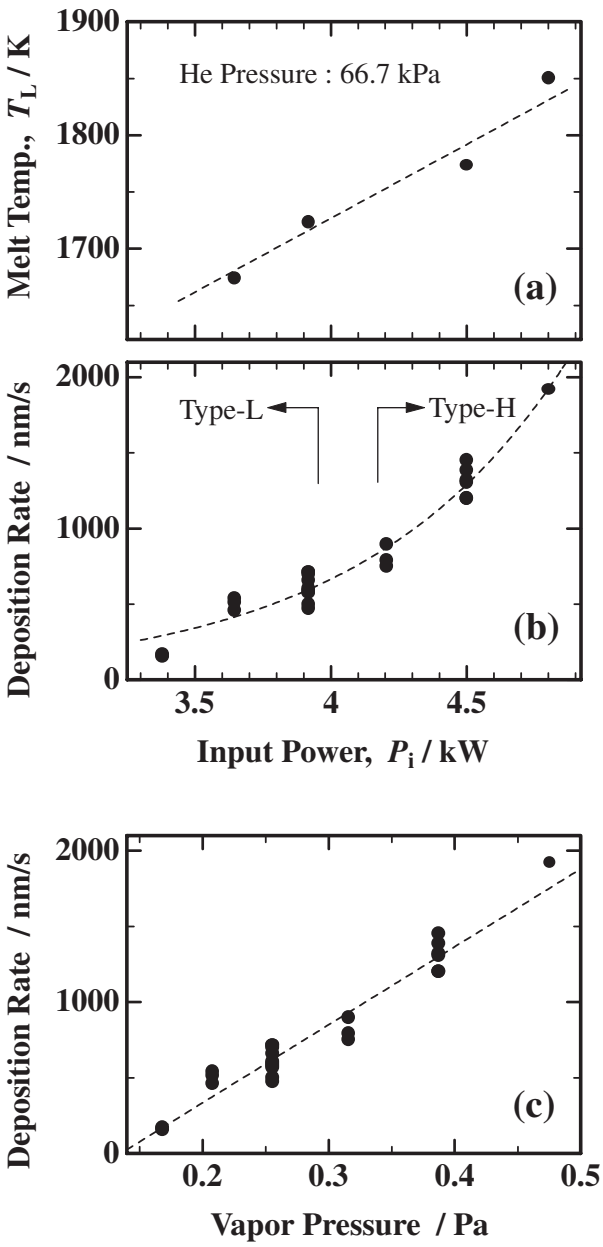

Fig. 1 (a) Au melt temperature, T_L, and (b) deposition rate as a function of the input RF-power, P_i. (c) Deposition rate against the vapor pressure of Au. The dashed lines are depicted to guide eyes.

A preliminary positron lifetime study was conducted for the n-Au specimens in the as-prepared state. The lifetime spectra could be explained by two constituents with the lifetimes of τ_{p1} and τ_{p2}. The value of about 185 ps for τ_{p1} is similar to the positron lifetime in single vacancies. The value of about 350 ps for τ_{p2} corresponds to the positron lifetime in micro aggregates of a few vacancies. The long lifetime component associated with pores was not detected. The intensity ratio, I_{p1}/I_{p2}, of the τ_{p1} component to the τ_{p2} component was about 9/1, indicating that most of the vacancy-type defects contained in the present n-Au specimens are of a single vacancy type. Ito *et al.*[25] reported the positron lifetime spectra with similar τ_{p1} and τ_{p2} for n-Au specimens prepared by the GD method, however, the value reported for I_{p1}/I_{p2} is about 3/2 which is much smaller than 9/1 found for the present n-Au specimens. For the positron

lifetime spectra reported for various n-metal specimens prepared by the gas-condensation and compaction method, I_{p1}/I_{p2} is less than 3/2, and τ_{p2} is as large as micro voids containing 10 to 15 vacancies.[26,27]

The X-ray diffraction (XRD) measurements were made by using the Cu K_α radiation (40 kV, 30 mA), where the instrumental line broadening was corrected by using the spectra of Si powders. The XRD measurement in the θ–2θ scan mode was conducted with two different geometrical setups, *i.e.*, the XRD scattering (q-) vector was normal to or parallel to the specimen flat-surface (the $q_\perp$ or $q_\parallel$ conditions, hereafter). The XRD spectra measured under the $q_\perp$ and $q_\parallel$ conditions will be referred to as $I_\perp$ and $I_\parallel$, and the (hkl) reflection peak in $I_\perp$ as $I_{\perp(hkl)}$, respectively. The crystallites whose $\langle hkl\rangle$ direction is normal (or parallel) to the specimen flat-surface are referred to as the $\langle hkl\rangle_\perp$ (or $\langle hkl\rangle_\parallel$) crystallites, hereafter.

The annealing of the n-Au specimens was performed in a vacuum of 10^{-4} Pa for 1.8 ks. In order to avoid undesirable constraint during annealing, a ribbon of the n-Au specimen was sandwiched by two glass plates which were separated by a gap slightly larger than the specimen thickness. A change in the specimen length, $\Delta L/L_0$, due to annealing was measured as follows. Two small markers with a gage length, L, of about 20 mm were indented on the specimen flat-surface by the Vickers hardness tester, and a change in L due to annealing was measured at RT by using an optical microscope. The Vickers hardness, H_v, was measured under the loading of 0.098 N for 5 s at RT. The tensile tests were carried out using an Instron-type tensile apparatus in the temperature range between 80 K and 300 K. The vibrating reed measurements with a strain amplitude of about 10^{-6} were carried out at the resonant frequency of about 300 Hz in the temperature range between 10 K and 300 K. (See the previous work[17] for the apparatuses.)

3. Results

3.1 Characterization of n-Au specimens in the as-prepared state

As mentioned, the deposition rate of ultrafine Au particles on a substrate was controlled by adjusting P_i. Figure 1(b) shows the deposition rate as a function of P_i. Figure 1(c) is the redrawing of Fig. 1(b), but here the deposition rate is plotted against the vapor pressure of Au which is estimated from the T_L *vs.* P_i data shown in Fig. 1(a) and the thermodynamic data.[28] The deposition rate of ultrafine Au particles is increased linearly with the vapor pressure of Au in the present experimental condition. We shall refer to P_i instead of the deposition rate below. In Fig. 1(b), the classification of the n-Au specimens by the deposition rate is indicated, *i.e.*, the type-L specimens prepared at P_i below 4 kW and the type-H specimens at P_i above 4 kW, respectively.

In Fig. 2(a), the density of the n-Au specimens in the as-prepared state is plotted as a function of P_i. Figure 2(b) shows the density measured for the n-Au specimens annealed at 1100 K for 1.8 ks and for that of a 5N p-Au foil with the similar size as a reference. All the values observed for the type-L specimens, the type-H specimens and the p-Au foil show good agreement with 19.32 g/cm^3 reported for the bulk Au value in literature.[28] The densities measured for the n-Au specimens are listed in Table 1.

Figures 3(a) and (b) show examples of the XRD spectra $I_\perp$ and $I_\parallel$ observed for the type-L specimens. $I_{\perp(111)}$ is strong, $I_{\perp(222)}$ moderate and $I_{\perp(200)}$, $I_{\perp(220)}$, $I_{\perp(311)}$ and $I_{\perp(331)}$ much weaker, while $I_{\parallel(111)}$, $I_{\parallel(200)}$, $I_{\parallel(220)}$, $I_{\parallel(311)}$ and $I_{\parallel(222)}$ reflections are consistent with those of a bulk powder specimen. It is not shown here but $I_\perp$ and $I_\parallel$ observed for the type-H specimens are similar to those observed for the type-L specimens except that the relative strengths for $I_{\parallel(hkl)}$ are different between the type-L and type-H specimens. Figure 4 shows the volume fraction of the $\langle hkl\rangle_\parallel$ crystallites, $R_{\parallel\langle hkl\rangle}$, found for the n-Au specimens as a function of P_i, where $R_{\parallel\langle hkl\rangle}$ for the predominant $I_{\parallel(200)}$, $I_{\parallel(220)}$ and $I_{\parallel(111)}$ reflections are plotted. $R_{\parallel\langle hkl\rangle}$ is estimated using the following equation,

$$R_{\parallel\langle hkl\rangle} = (A_{\parallel(hkl)}/F^2L^*)/\left[\sum_{\langle mno\rangle}(A_{\parallel(mno)}/F^2L^*)\right], \qquad (3)$$

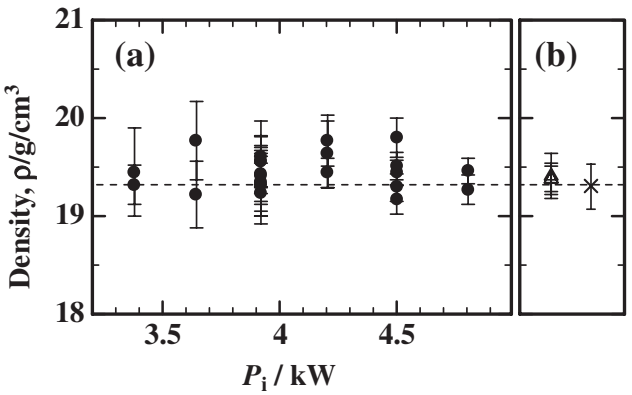

Fig. 2 (a) Density, ρ, of the n-Au specimens as a function of P_i. (b) ρ of the n-Au specimens found after annealing at 1100 K (open triangles) and ρ of a polycrystalline Au specimen (cross). The dashed horizontal line indicates the bulk Au density of 19320 kg/m^3.

Table 1 Structural characteristics and thermal stability of the n-Au specimens.

Specimen	Density (kg/m^3)	$\langle d\rangle$ (nm)			$3[(\Delta L/L_0)-(\Delta a/a_0)]_{400\,K}$[b]	T_{GG}[c] (K)
		d_{STM}[a]	$d_{S(111)}$[a]	d_{MWH}[a]		
Type-L	19400 ± 200	~20	~40	60–80	~15 × 10^{-4}	400–500
Type-H	19400 ± 200	~20	~40	—		300–400

[a] d_{STM}, $d_{\perp(111)}$ and d_{MWH}; mean grain size estimated from STM surface morphology, Scherrer analysis of the $I_{\perp(111)}$ reflection and the modified Williamson-Hall plot, respectively (see text).
[b] Concentration of the vacancy type defects found after annealing at 400 K.
[c] Onset temperature of grain growth for annealing time of 1.8 ks.

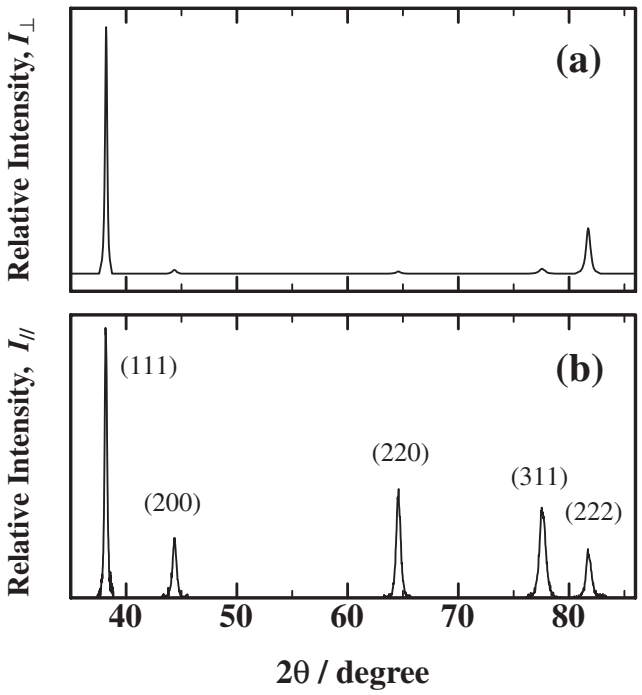

Fig. 3 Examples of the XRD spectra, I, observed for the type-L specimens: (a) $I_\perp$ and (b) $I_\parallel$.

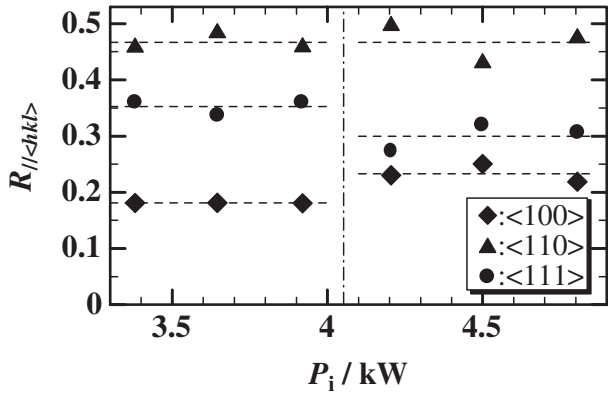

Fig. 4 $R_{\parallel\langle hkl\rangle}$ against P_i, where $R_{\parallel\langle hkl\rangle}$ denotes the volume fraction of the crystallites whose $\langle hkl\rangle$ direction is parallel to the specimen flat-surface.

where $A_{\parallel(hkl)}$ denotes the integrated intensity of $I_{\parallel(hkl)}$, F is the structure factor, and L^* is the Lorenz polarization factor. The results in Fig. 4 indicate that the values of $R_{\parallel\langle hkl\rangle}$ are different between the type-L and the type-H specimens, but remain constant among the each type.

The mean grain size in the n-Au specimens was estimated from the STM surface morphology and the peak broadening of the XRD reflections. Figure 5 shows an example of the STM images observed for the specimen flat-surface of the type-L specimens, where the sizes of dome-like swells are between 15 and 30 nm. The secondary agglomerates which were observed in the previous work,[22] pores and cracks are not found in the present specimens. STM images very similar to Fig. 5 were observed for the sectional surface of the type-L specimens, and also for the specimen flat-surface and the sectional surface of the type-H specimens. Figure 6(a) shows an example for the $q_\perp$ dependence of the line width, $\Delta q_\perp$, of

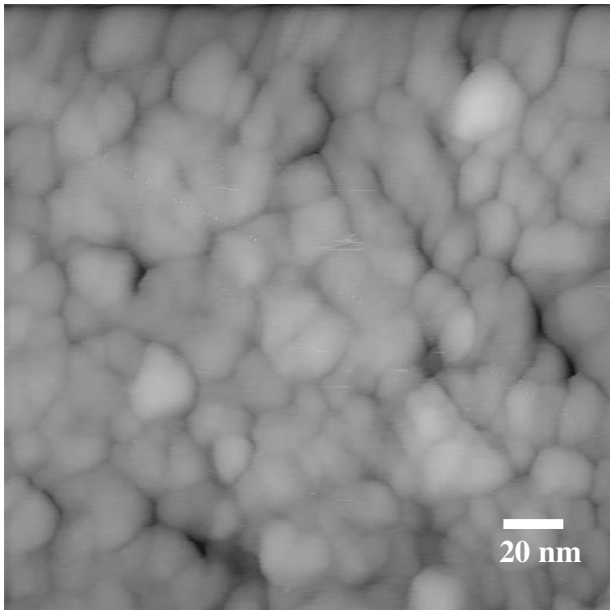

Fig. 5 STM surface image observed for the flat-surface of the type-L specimen ($P_i = 3.6$ kW).

the $I_{\perp(hkl)}$ reflections observed for the type-L specimens. As seen in Fig. 6(a), the $\Delta q_\perp$ *vs.* $q_\perp$ data cannot be explained by a linear relationship (the Williamson-Hall analysis), indicating that the mean grain size and/or internal strain are considerably different among the various $\langle hkl\rangle_\perp$ crystallites. Figure 6(b) is a redrawing of Fig. 6(a), but here the modified Williamson-Hall analysis[29,30] is applied to the data, where C is a contrast factor reflecting the strain anisotropy. The $\Delta q_\perp$ *vs.* $q_\perp C^{0.5}$ plot shown in Fig. 6(b) can be explained assuming that the mean grain size is similar among the various $\langle hkl\rangle_\perp$ crystallites, and falls between 60 and 80 nm which is about three times larger than that found in the STM images. On the other hand, as shown in Fig. 3, the fractional volumes of the $\langle 100\rangle_\perp$, $\langle 110\rangle_\perp$, $\langle 311\rangle_\perp$ and $\langle 331\rangle_\perp$ crystallites are much smaller than that of the $\langle 111\rangle_\perp$ crystallites, indicating that the $\langle 100\rangle_\perp$, $\langle 110\rangle_\perp$, $\langle 311\rangle_\perp$ and $\langle 331\rangle_\perp$ crystallites are embedded in the matrix of the $\langle 111\rangle_\perp$ crystallites. In such a case, the mean grain size for the $\langle 100\rangle_\perp$, $\langle 110\rangle_\perp$, $\langle 311\rangle_\perp$ and $\langle 331\rangle_\perp$ crystallites are not the same as the $\langle 111\rangle_\perp$ crystallites. It is noted that the application of the Scherrer's equation gives about 40 nm for the mean grain sizes of the $\langle 111\rangle_\perp$ crystallites and about 20 nm for the $\langle 100\rangle_\perp$ crystallites, respectively (see Fig. 9), which show good agreement with the grain sizes found in the STM images. Figure 7 is the $q_\perp$ dependence of $\Delta q_\perp$ observed for the type-H specimens. The $\Delta q_\perp$ *vs.* $q_\perp$ data observed for the type-H specimens cannot be explained by the modified Williamson-Hall analysis with a single parameter (not shown here). The result shown in Fig. 7 suggests that in the type-H specimens, a distribution of internal strains and/or the mean grain size is considerably different among the various $\langle hkl\rangle_\perp$ crystallites. Applying the Scherrer's equation to the data shown in Fig. 7, we find that the mean grain sizes of the $\langle 111\rangle_\perp$ and the $\langle 100\rangle_\perp$ crystallites are about 40 nm and the internal strains may be different between these crystallites. It is noted that the mean grain sizes found in Fig. 7 show good agreement with the grain

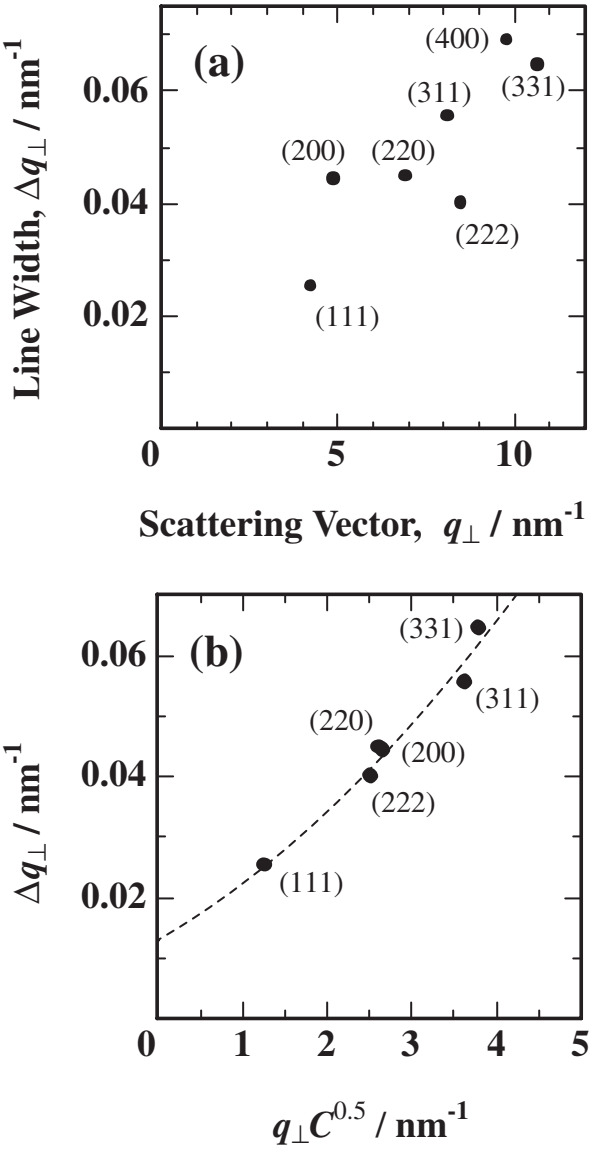

Fig. 6 (a) Scattering vector, $q_\perp$, dependence in the line width, $\Delta q_\perp$, (the Williamson-Hall plot) observed in the XRD spectra for the type-L specimen ($P_i = 3.9$ kW). (b) Repotting of the data in (a) according to the modified Williamson-Hall analysis.

sizes found in the STM images. In the present study, the mean grain sizes were determined for the predominant $\langle 111 \rangle_\perp$ crystallites by using the Scherrer's equation. The grain sizes estimated from the STM images and the XRD spectra are listed in Table 1.

We shall discuss a process for branching off of the specimens briefly. As shown in Fig. 3, the $\langle 111 \rangle_\perp$ crystallite is predominant among various $\langle hkl \rangle_\perp$ crystallites for both the type-L and type-H specimens, indicating that ultrafine Au particles undergo a certain rearrangement on the specimen flat surface just after landing. On the other hand, the $R_{\parallel \langle hkl \rangle}$ data shown in Fig. 4 suggest that the degree of rearrangement is not the same between the type-L and type-H specimens, where the rearrangement may not be completed for the type-H specimens because of the higher deposition rates. Referring to the deposition rate shown in Fig. 1(b), the lower bound of the deposition rate for the type-H specimens is about 800 nm/s, which corresponds to the top on top

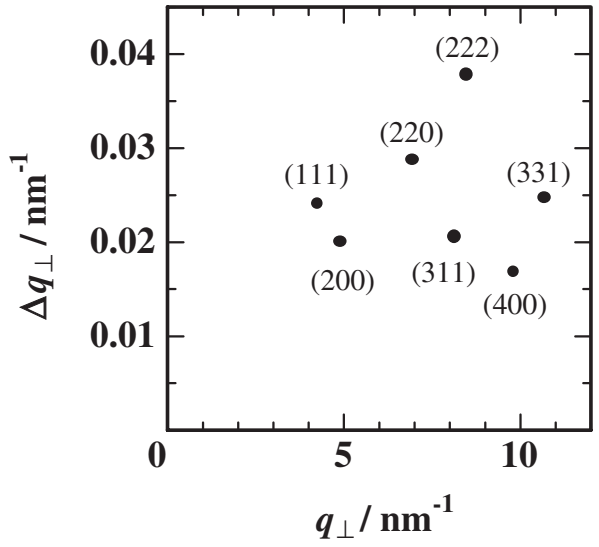

Fig. 7 $q_\perp$ dependence in $\Delta q_\perp$ (the Williamson-Hall plot) observed in the XRD spectra for the type-H specimen ($P_i = 4.4$ kW).

stacking rate of about 76 particle/s or the arrival time interval of about 0.013 s when the dense packing of the ultrafine Au particles with 20 nm diameter is assumed. The detailed process of the relaxation is out of the present scope.

Figures 8(a) and (b) show examples of the changes in the relative intensities of $I_{\perp(hkl)}$ by annealing observed for the type-L and the type-H specimens, respectively. The annealing was carried out at the desired temperature, T_{ann}, for 1.8 ks. For the type-L specimens, $I_{\perp(111)}$ is predominant even after annealing at 1100 K (the data for $T_{ann} > 700$ K are not shown

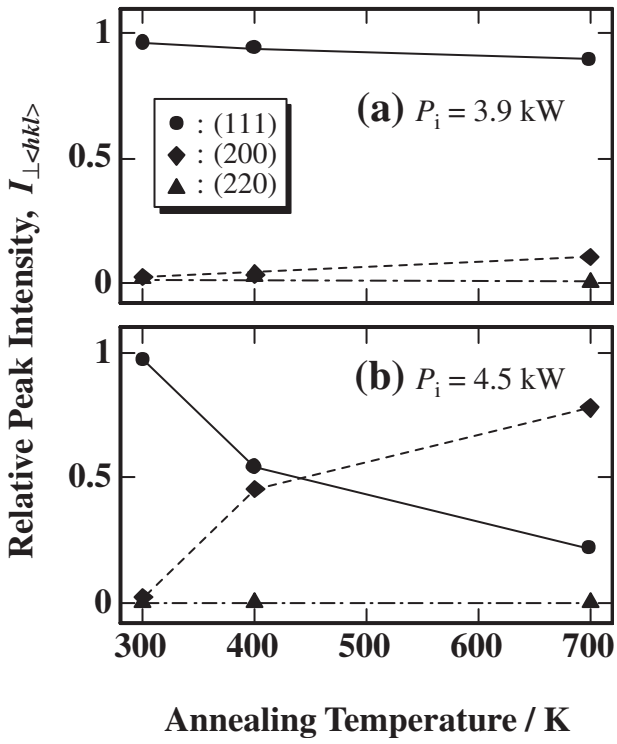

Fig. 8 Changes in the relative intensities of $I_{\perp(hkl)}$ after annealing: (a) for the type-L specimen ($P_i = 3.6$ kW) and (b) for the type-H specimen ($P_i = 4.5$ kW).

here). In contrast, a strong increase in $I_{\perp(200)}$ and a complimentary decrease in $I_{\perp(111)}$ were observed for the type-H specimens after annealing. Figures 9(a), (b) and (c) show changes in the grain size $d_{\perp\langle hkl\rangle}$ and the Vicker's hardness, H_v, as a function of T_{ann}, where $d_{\perp\langle hkl\rangle}$ is estimated from the $I_{\perp(hkl)}$ reflection by applying the Scherrer's equation. It is noted that H_v of the n-Au specimens decreases with increasing the mean grain size in the present range.[17] As seen in Figs. 9(a) to (c), the onset temperature of grain growth, T_{GG}, is in the range between 400 and 500 K for the type-L specimens and between 300 and 400 K for the type-H specimens, respectively. The values of T_{GG} observed for the type-L and type-H specimens are listed in Table 1.

We carried out differential scanning calorimetry (DSC) measurements of the n-Au specimens, where a continuous energy release was observed during warm-up from 350 to 750 K. A total energy release between 350 and 750 K was $(5 \pm 2) \times 10^2$ J/mol for both the type-H and type-L specimens. As seen in Fig. 9, the grain growth proceeds between 350 K and 700 K. The assumption that the energy release of $(5 \pm 2) \times 10^2$ J/mol reflects the reduction of the GB regions gives the GB energy of (0.3 ± 0.15) J/m^2 for the n-Au specimens with the grain size of 20 nm, which is comparable with 0.45 J/m^2 reported for the bulk Au at RT.[31] It is noted that for n-Ni prepared by the electrodeposition method, the energy release of 415.7 J/mol was observed at around 606 K and attributed to the reduction of the GB regions by the grain growth.[32]

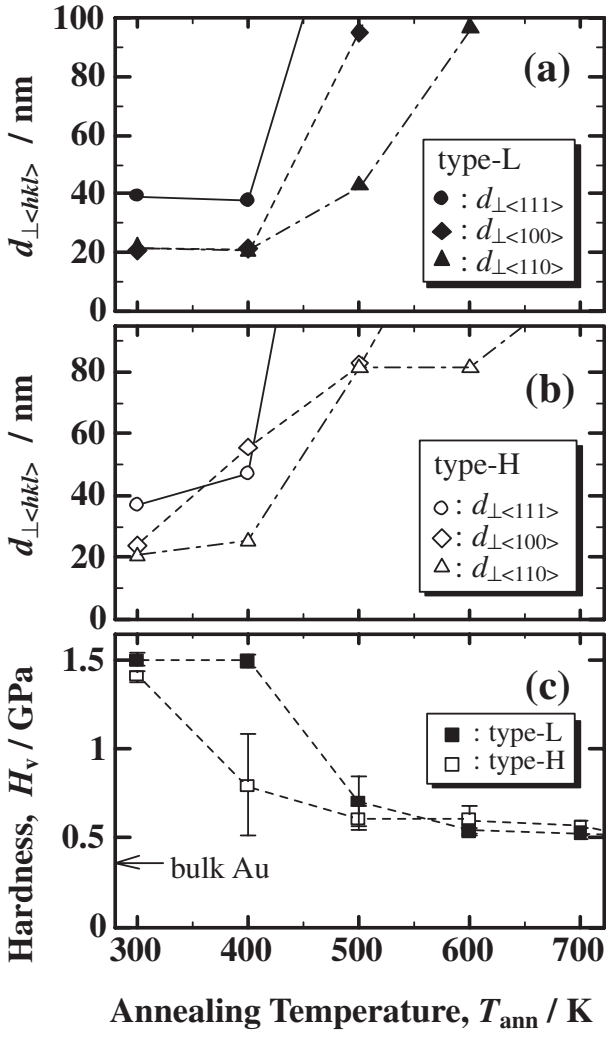

Fig. 9 (a) Mean grain size, $d_{\perp\langle 111\rangle}$, $d_{\perp\langle 100\rangle}$ and $d_{\perp\langle 110\rangle}$, against T_{ann} observed for the type-L specimen ($P_i = 3.6$ kW). (b) $d_{\perp\langle 111\rangle}$, $d_{\perp\langle 100\rangle}$ and $d_{\perp\langle 110\rangle}$ against T_{ann} observed for the type-H specimen ($P_i = 4.5$ kW). (c) Vicker's hardness, H_v, against T_{ann}, observed for the type-L (filled squares) and type-H (open squares) specimens.

3.2 Mechanical responses of the n-Au specimens

Figures 10(a) and (b) show examples of the stress-strain curve observed for the type-L and type-H specimens at the strain rate of 4.5×10^{-4} s^{-1}, respectively. The loading and unloading processes were successively made in the elastic region at temperatures between 80 to 300 K. For both the type-L and type-H specimens, the stress-strain curve observed at 77 K showed the linear elasticity and that at RT revealed a hysteresis between the loading and unloading runs which showed a complete recovery after a prolonged elapsed time. In the present tensile tests, the Young modulus was evaluated from the linear part in the stress-strain curve observed during loading. The Young modulus of the n-Au specimens was also evaluated by means of the vibrating reed method at the resonant frequency of ~300 Hz in the temperature range between 10 and 300 K. Figure 11 shows the Young modulus as a function of temperature observed for

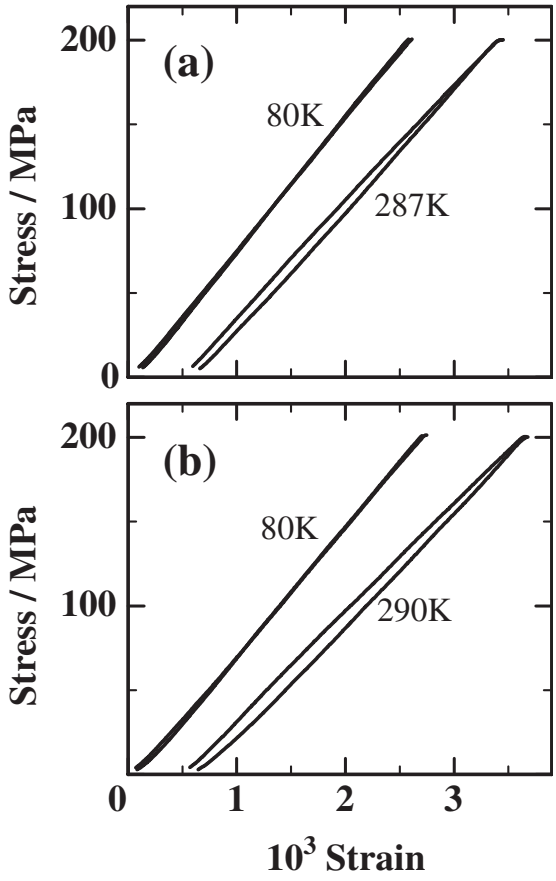

Fig. 10 Stress-strain curves observed for (a) the type-L specimen ($P_i = 3.9$ kW) at 80 K and room temperature (RT), and (b) the type-H specimen ($P_i = 4.5$ kW), where the curve observed at RT is shifted on the strain axis.

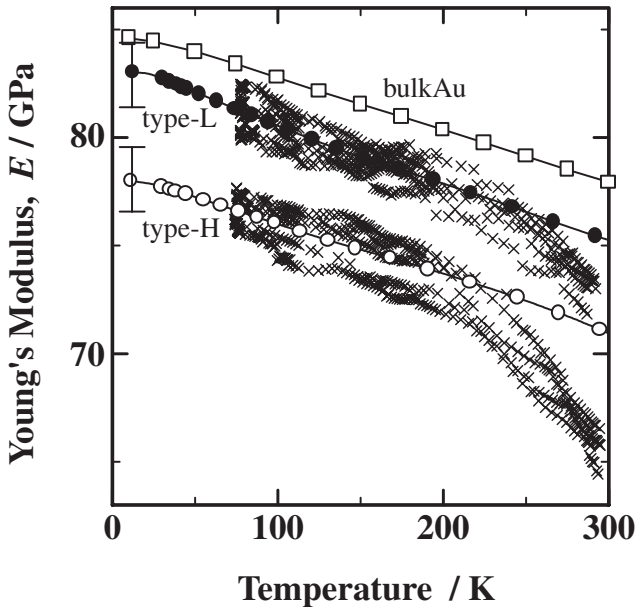

Fig. 11 Temperature change in the Young modulus observed for the n-Au specimens. The crosses denote the tensile test data for four type-L specimens ($P_i = 3.9$ kW) and seven type-H specimens ($P_i = 4.5$ kW). The filled and the open circles denote the vibrating reed data for the type-L and the type-H specimens, respectively. The open squares denote the Young modulus estimated for a randomly oriented polycrystalline bulk Au under Hill's assumption.

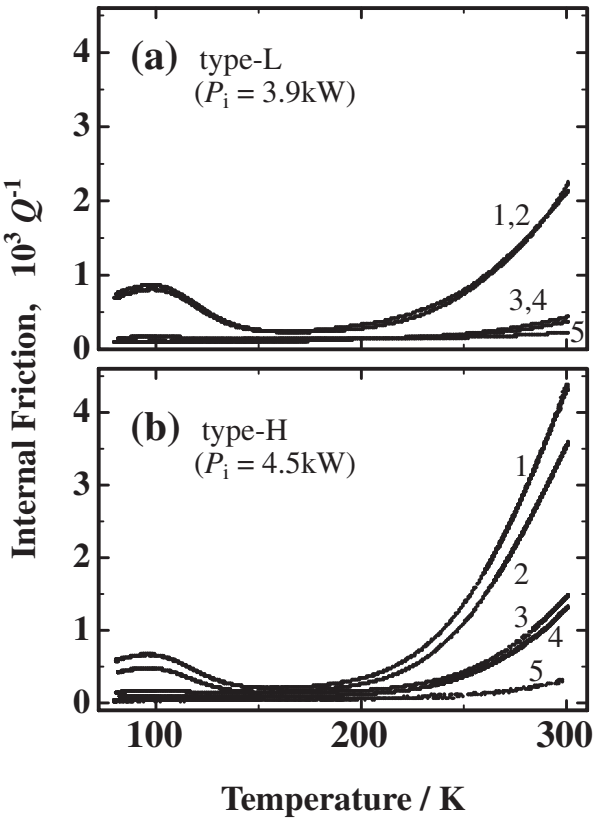

Fig. 12 Temperature spectra of the internal friction, Q^{-1}, observed for the n-Au specimens. (a) The type-L specimen ($P_i = 3.9$ kW) and (b) the type-H specimen ($P_i = 4.5$ kW), where the curves 1 to 5 were observed in the as-deposited state, after annealing at 400, 500, 600 and 1100 K, respectively.

the type-L and the type-H specimens, where both the data from the tensile test in the strain range of 10^{-3} and from the vibrating reed measurements in the strain range of 10^{-6} are depicted. It is noted that in Fig. 11, the data from the vibrating reed measurements are calibrated to the mean value of the data from the tensile tests at 80 K, where the amount of calibration is smaller than the experimental error. The temperature dependence of the Young modulus of both the type-L and -H specimens are similar to that reported for the poly-Au below 200 K. As shown in Fig. 11, the Young modulus of both the type-L and -H specimens shows a decrease from the parallelism with that of the poly-Au above 200 K, where the decrease is larger for the tensile test data than for the vibrating reed measurement data. That is, the anelastic strain revealed above 200 K, $\varepsilon_{an,>200\,K}$, is composed of $\varepsilon_{an,>200\,K}$-I and $\varepsilon_{an,>200\,K}$-II, where $\varepsilon_{an,>200\,K}$-I is the linear anelastic strain responsible for the decrease in the Young modulus observed with a strain amplitude of 10^{-6} and $\varepsilon_{an,>200\,K}$-II is revealed for the applied stress beyond a few MPa with the distributed relaxation times (see Fig. 10 and Ref. 6)).

Figures 12(a) and (b) show changes in the internal friction of the type-L and type-H specimens after annealing, where the strain amplitude used is 10^{-6}. The relaxation peak at around 95 K (the 95 K Q^{-1}-peak) and the rapid increase above 200 K ($Q^{-1}_{>200\,K}$) are observed in the as deposited state. The 95 K Q^{-1}-peak and $Q^{-1}_{>200\,K}$ diminish after annealing at 500 K, where the grain growth is strongly progressed (see Fig. 9). These features indicate that both the 95 K Q^{-1}-peak and $Q^{-1}_{>200\,K}$ are associated with anelastic processes in the GB regions. We surmise that $\varepsilon_{an,>200\,K}$-I is associated with $Q^{-1}_{>200\,K}$. Further, $\varepsilon_{an,>200\,K}$-II is also associated with a certain anelastic process in the GB regions because it can be observed in n-Au specimens but not in poly-Au specimens. A certain characteristic process associated with several atoms in the GB of the n-metals appears to be responsible for $\varepsilon_{an,>200\,K}$-I and $\varepsilon_{an,>200\,K}$-II,[6,33] however, the detailed mechanisms are not known at the present.

4. Discussion

4.1 Vacancy type defect in high-density n-Au

It is known that, when Schottky-type defects are introduced in materials, the specific volume shows a slight increase. Simmons and Balluffi[34] carried out the simultaneous measurements of the fractional changes in the lattice parameter, $\Delta a/a_0$, and the specimen length, $\Delta L/L_0$, during heating, and succeeded to evaluate the equilibrium concentration of thermal vacancies, $C_v^{(eq)}$, as a function of the specimen temperature as,

$$C_v^{(eq)} = 3(\Delta L/L_0 - \Delta a/a_0)^{(eq)}. \quad (4)$$

As already mentioned, the preliminary positron study suggests that the present n-Au specimens in the as-prepared state contain the vacancy type defects whose concentration, C_v, may be comparable with $C_v^{(eq)}$ near the melting temperature. If it is the case, C_v should decrease after annealing. Experimentally, one can expect a parallel change between $\Delta L/L_0$ and $\Delta a/a_0$ for annealing out of internal

stresses, and an opposite change between $\Delta L/L_0$ and $\Delta a/a_0$ for a variation in C_v. Then, C_v can be estimated from the simultaneous measurements of $\Delta L/L_0$ and $\Delta a/a_0$ at a given temperature after annealing by using the following equation,

$$C_v = 3(\Delta L/L_0 - \Delta a/a_0). \quad (5)$$

Figures 13(a) and (b) show $\Delta a/a_0$ and $\Delta L/L_0$ observed at RT for the type-L and the type-H specimens as a function of T_{ann}, respectively, where a_0 is the bulk lattice constant and L_0 is the length found after annealing at 1100 K. In order to improve the accuracy, a is determined by applying Nelson-Riley's function[35] to the $I_\perp$ data. Figure 13(c) shows a change in $3(\Delta L/L_0 - \Delta a/a_0)$ found for two type-L specimens and one type-H specimen. For both the type-L and type-H specimens, $3(\Delta L/L_0 - \Delta a/a_0)$ shows an increase for T_{ann} and then a decrease for T_{ann} between 400 and 700 K. We surmise that the increase found between 300 and 400 K is associated with an increase of vacancy type defects due to a relaxation of internal strains, and that the decrease observed between 400 and 700 K is associated with annealing out of vacancy type defects by the grain growth. The increase in $3(\Delta L/L_0 - \Delta a/a_0)$ at T_{ann} between 300 and 400 K is compatible with the view that the excess vacancy type defects are associated with the structural relaxation before the grain growth.[8,9] It is noted that for n-Cu prepared by the electrodeposition method, a small energy release of 3.2 J/mol was observed at around 423 K and supposed to reflect a recovery of the stored strains.[36] Then, we estimate C_v in the n-Au specimens after annealing at 400 K as about 15×10^{-4}, assuming that an atomic volume of the vacancy type defect is the same to that of a lattice vacancy. It is noted that C_v of 15×10^{-4} is the same order of the thermal vacancy concentration in bulk Au just below T_m. For n-Ni specimens prepared by sputtering, Liu *et al.*[37] observed a significant increase in a by 20×10^{-4} in $(\Delta a/a)$ after annealing and considered that annealing out of vacancy type defects was responsible for it. The increase in $(\Delta a/a_0)$ observed in the present n-Au specimens by annealing is about 5×10^{-4}, suggesting that C_v in the present n-Au specimens is lower than that in the n-Ni specimens prepared by sputtering.

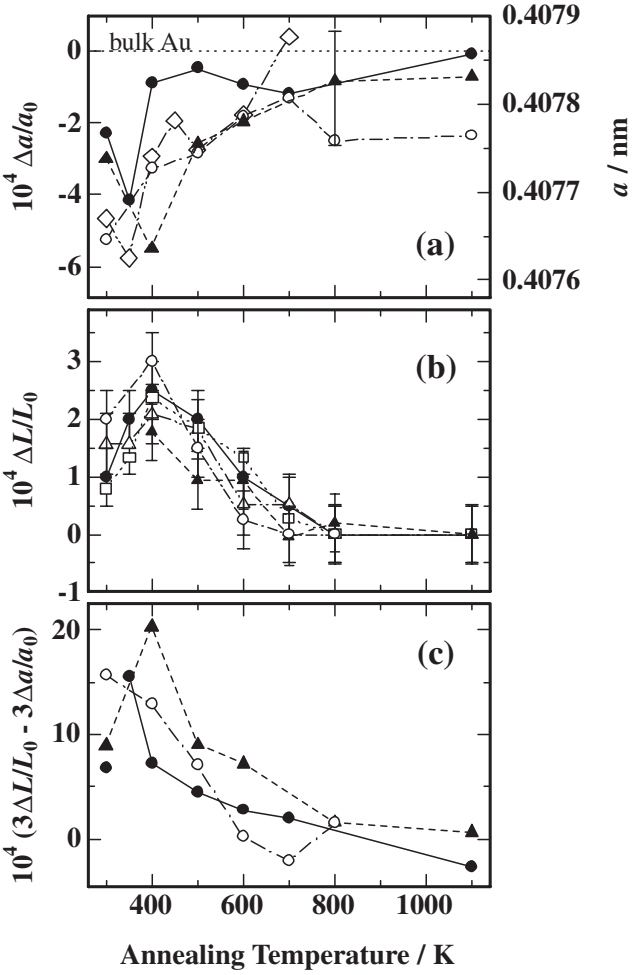

Fig. 13 (a) Changes in the lattice constant, a, against T_{ann} observed for the type-L (filled symbols) and type-H (open symbols) specimens. (b) Changes in the normalized specimen length, $\Delta L/L_0$, against T_{ann} observed for the type-L (filled symbols) and type-H (open symbols) specimens. (c) $3(\Delta L/L_0 - \Delta a/a_0)$ *vs.* T_{ann} (see text).

The Vicker's Hardness data shown in Fig. 9(c) indicate that the grain growth of the n-Au specimens strongly progresses between 350 K and 500 K and gradually at elevated temperatures. Except for the increase in $3(\Delta L/L_0 - \Delta a/a_0)$ at T_{ann} between 300 and 400 K, the decrease in C_v by annealing appears to be parallel to the increase in the grain size. This parallelism suggests that most of vacancy-type defects are in the GB regions. The retardation of the grain growth was reported for n-Fe specimens prepared by ball-milling,[7] and we observed the retarded grain growth for the n-Au films prepared by sputtering method.[38] We surmise that the grain growth of n-metals are governed by the properties of the GB regions.

4.2 Young modulus and deformation mode of high-density n-Au

In Fig. 11, the Young modulus at 10 K, $E_{obs,10\,K}$, is found to be 83 ± 1.5 GPa for the type-L specimen and 78 ± 1.5 GPa for the type-H specimens, respectively, and these values are compiled in Table 2. Firstly, an effect of the lattice dilatation on the Young modulus is taken into account. From the Mössbauer spectroscopy of n-Fe particles,[39] it is reported that a decrease in the Debye temperature and an increase in the lattice constant from the bulk values are found with decreasing the size. From the computer simulation for the structural and elastic properties of Cu–Ni thin multilayers,[40] the increase in the Young modulus with decreasing the lattice constant is reported. The fractional change in the Young modulus, $(\Delta E/E_0)_{dila}$, due to the lattice dilatation, $(\Delta a/a_0)_{dila}$, can be estimated as $(\Delta E/E_0)_{dila} = -16(\Delta a/a_0)_{dila}$ for n-Fe particles[39] and $(\Delta E/E_0)_{dila} = -14(\Delta a/a_0)_{dila}$ for Cu–Ni thin multilayers[40] at $(\Delta a/a_0)_{dila} \ll 1$. Then, we assume the relationship of $(\Delta E/E_0)_{dila} = -15(\Delta a/a_0)_{dila}$ for the n-Au specimens. As seen in Fig. 13(a), $(\Delta a/a_0)$ in the as-deposited state is negative. By substituting $(\Delta a/a_0)_{dila}$ in the as deposited state to the relationship of $(\Delta E/E_0)_{dila} = -15(\Delta a/a_0)_{dila}$, one can find $(\Delta E/E_0)_{dila} = +4 \times 10^{-3}$ and $+7 \times 10^{-3}$ for the type-L and the type-H specimens, respectively. The proper Young modulus free from the dilatation effect, $(E_{0,10\,K})_{obs}$, is estimated after subtracting $(\Delta E/E_0)_{dila}$ from $E_{obs,10\,K}$ and the results are listed in Table 2.

Table 2 Elastic properties of the n-Au specimens.

Specimen	$E_{\mathrm{obs},10\,\mathrm{K}}$ (GPa)	$(E_{0,10\,\mathrm{K}})_{\mathrm{obs}}$ (GPa)	$(E_{0,10\,\mathrm{K}})_{\mathrm{Calc}}$ (GPa)		$\frac{(E_{0,10\,\mathrm{K}})_{\mathrm{obs}}}{{}^{\sigma}E_{0,10\,\mathrm{K}}}$	Reference
			${}^{\varepsilon}E_{0,10\,\mathrm{K}}$	${}^{\sigma}E_{0,10\,\mathrm{K}}$		
Type-L	83 ± 1.5	~82.6	93.9	83.4	0.99	present
Type-H	78 ± 1.5	~77.4	90.4	79.6	0.97	present
Previous	79 ± 4 (20 K)					17)

As already mentioned, the Young modulus, E_0, expected for a polycrystalline specimen may be found between ${}^{\sigma}E_0$ and ${}^{\varepsilon}E_0$ given by (1) and (2), respectively. For the type-L and type-H specimens, the theoretical values at 10 K, ${}^{\sigma}E_{0,10\,\mathrm{K}}$ and ${}^{\varepsilon}E_{0,10\,\mathrm{K}}$, may be estimated from the $R_{\parallel\langle hkl\rangle}$ data shown in Fig. 4 and the Young modulus at 10 K, $E_{\langle 100\rangle,10\,\mathrm{K}} = 46.5$ GPa, $E_{\langle 110\rangle,10\,\mathrm{K}} = 88.2$ GPa and $E_{\langle 111\rangle,10\,\mathrm{K}} = 125.7$ GPa, reported for Au metal.[19] The results are compiled in Table 2. As seen in Table 2, $(E_{0,10\,\mathrm{K}})_{\mathrm{obs}}$ is very close to ${}^{\sigma}E_{0,10\,\mathrm{K}}$ for both the type-L and type-H specimens, and that ${}^{\varepsilon}E_{0,10\,\mathrm{K}}$ is much higher than $(E_{0,10\,\mathrm{K}})_{\mathrm{obs}}$. It is noted that the Young modulus shows a decrease by about 0.7% and 2.5% for the type-L and the type-H specimens after annealing at 800 K, respectively. These decreases in the Young modulus can be explained by the change in the texture after annealing.[17] The larger decrease for the type-H specimens is compatible with the fact that the $\langle 100\rangle_{\perp}$ crystallites become predominant by the grain growth as shown in Fig. 8(b). Since both the 95 K Q^{-1}-peak and $Q^{-1}_{>200\,\mathrm{K}}$ come to diminish with the progress of the grain growth, they are due to probable anelastic processes in the GB regions. No increase in the Young modulus in spite of these changes by the grain growth may indicate that the Young modulus of the GB region in n-Au is very close to the bulk value. That is, $(E_{0,10\,\mathrm{K}})_{\mathrm{obs}}$ is very close to the theoretical value of the Young modulus of the n-Au specimens in which the Young modulus of the GB regions is the same to the bulk value. Further, the fact that $(E_{0,10\,\mathrm{K}})_{\mathrm{obs}}$ is very close to ${}^{\sigma}E_{0,10\,\mathrm{K}}$ for both the type-L and type-H specimens indicates that the theoretical value of the Young modulus of a n-metal specimen can be given by ${}^{\sigma}E_0$. As listed in Table 2, the ratio of $(E_{0,10\,\mathrm{K}})_{\mathrm{obs}}/{}^{\sigma}E_{0,10\,\mathrm{K}}$ found is 0.99 and 0.97 for the type-L and the type-H specimens, respectively.

5. Conclusion

The n-Au specimens with the full density were prepared by means of the gas deposition method. The XRD spectra indicate that ultrafine Au particles undergo some rearrangement on the specimen flat-surfaces just after landing during the deposition. Two types of n-Au specimens are prepared as a function of the deposition rate, the type-H specimens above 800 nm/s and the type-L specimens below 800 nm/s. We surmise that the rearrangement of the n-Au particles on the specimen surfaces is not completed for the type-H specimens. The grain growth starts between 300 K and 400 K for the type-H specimens and between 400 K and 500 K for the type-L specimens, respectively. Preliminary DSC measurements show a continuous energy release by $(5 \pm 2) \times 10^2$ J/mol between 350 K and 750 K for both the type-H and type-L specimens. The GB energy estimated is (0.3 ± 0.15) J/m^2 which is comparable with 0.45 J/m^2 reported for bulk p-Au. The concentration of excess vacancy type defects, C_{v}, appears to increase to about 15×10^{-4} due to the complementary decrease in internal strains after annealing at 400 K, where an atomic volume of the vacancy type defects is assumed to be that of a lattice vacancy. C_{v} decreases with increasing annealing temperature and diminish after annealing at 800 K. For the mechanical property, it is indicated that the Young modulus of n-fcc-metals is explained by ${}^{\sigma}E$. The Young modulus observed at 10 K is $0.97{}^{\sigma}E$ and $0.99{}^{\sigma}E$ for the type-H and the type-L specimens, respectively, indicating that the Young modulus of the grain boundary regions is comparable with that of bulk Au. The Young modulus of both the type-L and -H specimens shows a decrease from the parallelism with that of the poly-Au above 200 K due to the anelastic processes in the GB regions.

Acknowledgments

The authors indebted to Prof. Y. Shirai at Osaka University for the positron life time studies. This work is partly supported by the Center for Tsukuba Advanced Research Alliance (TARA) at University of Tsukuba, a Grant in Aid for Scientific Research from the Ministry of Education, Culture, Sports, Science and Technology of Japan, and High Damping Materials Project of ''Research for the Future'' of Japan Society for the Promotion of Science.

REFERENCES

1) H. Gleiter: Prog. Mater. Sci. **33** (1989) 223–315.
2) E. F. Kneller and R. Howing: IEEE Trans. Magn. **MAG-27** (1991) 3588.
3) L. Lu, M. L. Sui and K. Lu: Science **287** (2000) 1463–1466.
4) S. Okuda and F. Tang: Nanostructured Mater. **6** (1995) 585–588.
5) R. Würschum, K. Reimann and P. Farber: Defect Diff. Forum **143–147** (1997) 1463–1468.
6) S. Sakai, H. Tanimoto, K. Otsuka, T. Yamada, Y. Koda, E. Kita and H. Mizubayashi: Scr. Mater. **45** (2001) 1313–1319.
7) C. E. Krill III, L. Helfen, D. Michels, H. Natter, A. Fitch, O. Masson and R. Birringer: Phys. Rev. Lett. **86** (2001) 842–845.
8) Y. Estrin, G. Gottestein and L. S. Shvindlerman: Acta Mater. **47** (1999) 3541–3549.
9) Y. Estrin, G. Gottestein, E. Rabkin and L. S. Shvindlerman: Scr. Mater. **43** (2000) 141–147.
10) G. W. Nieman, J. R. Weertman and R. W. Siegel: Scr. Metall. **23** (1989) 2013–2018.
11) D. Korn, A. Morsch, R. Birringer, W. Arnold and H. Gleiter: J. de Phys. **49** (1988) C5–769.
12) M. Weller, J. Diehl and H.-E. Schaefer: Philos. Mag. A **63** (1991) 527–533.
13) P. G. Sanders, A. B. Witney, J. R. Weertman, R. Z. Valiev and R. W. Siegel: Mater. Sci. Eng. **A204** (1995) 7–11.
14) P. G. Sanders, J. A. Eastman and J. R. Weertman: Acta Mater. **45** (1997) 4019–4025.
15) P. G. Sanders, C. J. Youngdahl and J. R. Weertman: Mater. Sci. Eng. **A234–236** (1997) 77–82.
16) X. Y. Qin, X. R. Zhang, G. S. Cheng and L. D. Zhang: Nanostruct. Mater. **10** (1998) 661–672.
17) S. Sakai, H. Tanimoto and H. Mizubayashi: Acta Mater. **47** (1999) 211–217.
18) H. S. Cao, J. J. Hunsinger and O. Elkedim: Scr. Mater. **46** (2002) 55–60.
19) G. Simmons and H. Wang: Single Crystal Constants and Calculated

Aggregate Properties: A HANDBOOK, 2nd ed., (M.I.T. Press, Cambridge, 1971).
20) S. Katsu, E. Fuchita, T. Tanabe and C. Hayashi: Jpn. J. Appl. Phys. **23** (1984) L910–912.
21) E. Fuchita, M. Oda and C. Hayashi: Materia Japan **34** (1995) 455–460.
22) H.Tanimoto, H. Fujita, H. Mizubayashi, Y. Sasaki, E. Kita and S. Okuda: Mater. Sci. Eng. A **217/218** (1996) 108–111.
23) A. H. Shapiro: *The Dynamics and Thermodynamics of Compressible Fluid Flow*, (Ronald Press, 1954).
24) W. C. Hinds: *Aerosol Technology* (John Wiley and Sons, New York, 1982).
25) Y. Ito, S. Takamura and M Kobiyama: Phys. Status Solidi (a) **179** (2000) 297–303.
26) R. Würschum, W. Greiner and H.-E. Schaefer: Nanostruct. Mater. **2** (1993) 55–62.
27) H.-E. Schaefer, R. Würschum, T. Gessmann, G. Stöckl, P. Scharwaechter, W. Frank, R. Z. Valiev, H.-J. Fecht and C. Moelle: Nanostruct. Mater. **6** (1995) 869–872.
28) *Smithells Metals Reference Book 6th ed.*, edited by E. A. Brandes, (Butterworth, London, 1983).
29) T. Ungár and A. Borbély: Appl. Phys. Lett. **69** (1996) 3173–3175.
30) T. Ungár, S. Ott, P. G. Sanders, A. Borbély and J. R. Weertman: Acta Mater. **46** (1998) 3693–3699.
31) J. M. Howe: *Interfaces in Materials*, (Wiley, New York, 1997), p. 308.
32) N. Wang, Z. Wang, K. T. Aust and U. Erb: Acta Metall. **45** (1997) 1655–1669.
33) H. Tanimoto, S. Sakai and H. Mizubayashi: Mater. Trans., in press.
34) R. O. Simmons and R. W. Ballufi: Phys. Rev. **117** (1960) 52–61.
35) H. P. Klug and L. E. Alexander: *X-ray Diffraction Procedures: for Polycrystalline and Amorphous Materials 2nd ed.*, (Wiley, New York, 1974).
36) L. Lu, N. R. Tao, L. B. Wang, B. Z. Ding and K. Lu: J. Appl. Phys. **89** (2001) 6408–6414.
37) X. D. Liu, Y. H. Zhang, K. Lu and Q. Z. Hu: J. Phys. Condens. Matter **6** (1994) L497–L502.
38) H. Tanimoto, Y. Koda, S. Sakai, E. Kita and H. Mizubayashi: *Proc. of the 22nd Riso International Symposium on Materials Science: Science of Metastable and Nanocrystalline Alloys, Structure, Properties and Modelling*, ed. by A. R. Dinesen *et al.*, (Riso National Laboratory, Roskilde, Denmark, 3–7 Sept., 2001) p. 401–406.
39) J. R. Childress, C. L. Chien, M. Y. Zhou and P. Scheng: Phys. Rev. B **44** (1991) 11689–11696.
40) R. S. Jones, J. A. Slotwinski and J. W. Mintmire: Phys. Rev. B **45** (1992) 13624–13630.